Proceedings of
The 1996 ASME Design Engineering Technical Conferences and
Computers in Engineering Conference
August 18-22, 1996, Irvine, California

96-DETC/CIE-1628

A COMBINED ANALYTICAL AND NUMERICAL APPROACH FOR THE SOLUTION OF AN EDGE LOADED SEMI-INFINITE ELASTIC SHEET

Xin Sun
Edison Welding Institute
Columbus, Ohio 43220
U.S.A.

Dale G. Karr
Department of Naval Architecture and
Marine Engineering
Ann Arbor, Michigan 48109-2145
U.S.A.

Chunhui Han
Liaoning Institute of Environmental Protection
Shenyang, Liaoning 110031
P.R. China

ABSTRACT

Edge loading of an semi-infinite elastic sheet is of interest to many engineering applications. In this paper the penetration problem involving a rigid indentor and an elastic semi-infinite sheet of uniform thickness is addressed using a combined analytical and numerical approach. The tenth-order approximate theory of stretching of an isotropic sheet is applied to formulate the governing differential equations. Solutions are then obtained using Fourier transforms for various loading conditions and numerical schemes are employed to calculate the three dimensional state of stress throughout the sheet. The influence of the aspect ratio on the resulting stress state is studied. Limit solutions for thin sheet and thick sheet are presented. Finite element analyses of the same loading conditions are also performed. Results are compared with those of the tenth-order theory and the stress distribution assumptions of the tenth-order theory are examined.

INTRODUCTION

Solution for the state of stress in an edge loaded semi-infinite plate or sheet is a typical elasticity problem and it is also of interest to many engineering applications such as offshore engineering and environmental engineering. For example, the solution of this problem could serve as an elastic approximation for the indentation process between ice sheets and offshore structures (Karr and Sun, 1995). When the plate is extremely thin or thick, the problem is often idealized to a two dimensional plane stress or plane strain problem and the solutions are readily presented in most elasticity text books such as Elasticity (Barber, 1992). Here, we consider the three dimensional indentation problem in which the homogeneous and isotropic sheet is bounded by two parallel planes $z = \pm c$ which are considered traction free, see Fig. 1. The tenth-order theory derived by Reissner and Clark (Reissner, 1942; Clark and Reissner, 1984) uses a set of two-dimensional differential equations for approximating the three dimensional Poisson's ratio corrections to the generalized plane stress theory of stretching of sheets. The problem with sheet subjected to normal varying sinusoidal loading has been studied by Clark (1985) using the tenth-order theory. Karr and Choi (1989) solved the problem with the applied stress being constant through the thickness of the sheet and extending from $x = -a$ to $x = a$. In this study, a similar approach is used and more general loading conditions are considered. Solutions are presented in the general form of Fourier transforms. Numerical solutions for three loading conditions are presented with solutions involving three Bessel functions of the first kind. More accurate schemes are applied to evaluate the Fourier transform and its inverse transform in order to get the converged three dimensional state of stress.

A study is presented of numerical results for the stresses that develop for various aspect ratios and various loading conditions. Solutions (for the stresses at the center of the loadings) are also obtained in the limit as the aspect ratio approaches zero. Clark (1985) obtained solutions for sinusoidally varying edge loading; analytic solutions for this loading were obtained for the limit condition as the thickness to wave length ratio approaches infinity. This limit condition is analogous to the condition for vanishing aspect ratio in this study. In contrast with what was presented in Karr and Choi (1989) for the limit solution, this study shows that the tenth-order theory is less accurate as the plate thickness increases (or as the width of loading decreases, i.e. knife loading). This is because the assumed stress variation across the thickness is no longer true, and therefore the limit solution does not converge to the plane strain solution.

GOVERNING DIFFERENTIAL EQUATIONS

In order to generalize the two dimensional plane stress solution to three dimensional sheet, Clark and Reissner (1984) assumed the stresses vary across the plate thickness in a parabolic variation. Since the upper and lower surfaces of the sheet are traction free, this assumption is compatible with equilibrium requirement and the boundary conditions. Based on these assumptions, the stress distributions are expressed in terms of stress resultants as:

$$(\sigma_x, \sigma_y, \tau_{xy}) = \frac{(N_{xx}, N_{yy}, N_{xy})}{2c} + \frac{(R_{xx}, R_{yy}, R_{xy})}{2c} Z''(z), \qquad (1)$$

$$(\tau_{xz}, \tau_{yz}) = \frac{1}{2c}(S_x, S_y) Z'(z), \qquad \sigma_z = -\frac{T}{2c} Z(z), \qquad (2)$$

where, $Z(z) = -\frac{c^2}{4}\left(1 - \frac{z^2}{c^2}\right)^2$, $Z'(z) = z\left(1 - \frac{z^2}{c^2}\right)$, $Z''(z) = 1 - 3\frac{z^2}{c^2}$.

The resulting governing differential equation for the stress field can be reduced to three uncoupled partial differential equations involving three stress functions φ, Ω and ψ (Clark, 1985):

$$\nabla^4 \varphi = 0, \qquad (3)$$

$$A_0 c^2 \nabla^2 \Omega - \Omega = 0, \qquad (4)$$

$$A_1 c^4 \nabla^4 \psi + A_2 c^2 \nabla^2 \psi + \psi = 0. \qquad (5)$$

The coefficients A_0, A_1 and A_2 for an isotropic sheet are given in the following (Clark and Reissner, 1984):

$$A_0 = \frac{2}{21}, A_1 = \frac{2}{63}\left(\frac{1 - 69\nu^2/70}{1 - \nu^2}\right), A_2 = -\frac{4}{21}. \qquad (6)$$

in which ν is the Poisson's ratio. The stress resultants on the right hand side of equations (1) and (2) are found by first introducing the auxiliary functions:

$$K(x, y) = \varphi - \frac{2\nu}{15} c^2 \psi, \qquad (7)$$

$$\chi(x, y) = \frac{2}{21}\left[(2 - \nu)\psi - \frac{1 - 69\nu^2/70}{3(1 + \nu)} c^2 \nabla^2 \psi\right] - \frac{\nu}{6(1 + \nu)} \nabla^2 \varphi. \qquad (8)$$

The equilibrium requirements for the stress resultants are then:

$$N_{xx} = \frac{\partial^2 K}{\partial y^2}, \qquad N_{yy} = \frac{\partial^2 K}{\partial x^2}, \qquad N_{xy} = \frac{\partial^2 K}{\partial x \partial y}, \qquad (9)$$

$$R_{xx} = \psi - c^2 \frac{\partial^2 \chi}{\partial y^2} + \frac{4c^2}{21} \frac{\partial^2 \Omega}{\partial x \partial y}, \; R_{yy} = \psi - c^2 \frac{\partial^2 \chi}{\partial x^2} - \frac{4c^2}{21} \frac{\partial^2 \Omega}{\partial x \partial y},$$
$$R_{xy} = c^2 \frac{\partial^2 \chi}{\partial x \partial y} + \frac{2c^2}{21}\left(\frac{\partial^2 \Omega}{\partial y^2} - \frac{\partial^2 \Omega}{\partial x^2}\right), \qquad (10)$$

$$S_x = -\frac{\partial \psi}{\partial x} - \frac{\partial \Omega}{\partial y}, S_y = -\frac{\partial \psi}{\partial y} + \frac{\partial \Omega}{\partial x}, T = -\nabla^2 \psi. \qquad (11)$$

From these equations we can see that, for a thin sheet, if one formally puts $c = 0$, then from equations (4) and (5), $\Omega = 0$, $\psi = 0$ and all quantities except N_{xx}, N_{yy}, N_{xy} vanish. $K = \varphi$ is a biharmonic function which represents the Airy stress function of elementary plane stress. As discussed in the following sections, edge loadings are considered which are applied over an edge distance of $2a$ (Fig. 1). The aspect ratio is defined as the ratio of the width of the loading to the sheet thickness, $\gamma = a/c$. For a thick plate, i.e. $c \gg a$, the aspect ratio γ approaches zero. Numerical solutions for a thick sheet have been obtained in this study as $\gamma \to 0$.

APPLIED TRACTIONS AND BOUNDARY CONDITIONS

We consider three kinds of loadings as illustrated in Fig. 2. General loading conditions can also be applied to the edge using the formulation shown below. The stress distributions along the plate edge corresponding to the three loading conditions are:

$$P_1(x) = \begin{cases} -\sigma_0(1-x^2/a^2) & (|x| \le a) \\ 0 & (|x| > a) \end{cases} \tag{12}$$

$$P_2(x) = \begin{cases} -\sigma_0(1-x^2/a^2)^{0.5} & (|x| \le a) \\ 0 & (|x| > a) \end{cases} \tag{13}$$

$$P_3(x) = \begin{cases} -\sigma_0(1-x^2/a^2)^{-0.5} & (|x| \le a) \\ 0 & (|x| > a) \end{cases} \tag{14}$$

The boundary conditions are the followings:

$$\sigma_y(x, 0, z) = P_j(x) \qquad j = 1, 2, 3 \tag{15}$$

$$\tau_{xy}(x, 0, z) = 0, \qquad \tau_{yz}(x, 0, z) = 0. \tag{16}$$

The edge tractions in equations (12)-(14) represent two dimensional parabolic stress distribution, the distribution corresponding to a frictionless rigid cylindrical indentor(2-D Hertz problem) and the distribution corresponding to a rigid flat indentor respectively (Timoshenko and Goodier, 1970; Barber, 1992).

Substituting of equation (1) into equation (15) yields:

$$\frac{1}{2c}N_{yy}(x, 0) + \frac{1}{2c}R_{yy}(x, 0)Z''(z) = P_j(x) \qquad j = 1, 2, 3 \tag{17}$$

Hence we have:

$$N_{yy}(x, 0) = 2c \cdot P_j(x), \tag{18}$$

$$R_{yy}(x, 0) = 0. \tag{19}$$

In addition, the shear stresses τ_{xy} and τ_{yz} must vanish on the boundary y=0 and therefore:

$$N_{xy}(x, 0) = 0. \tag{20}$$

$$R_{xy}(x, 0) = 0. \tag{21}$$

$$S_y(x, 0) = 0. \tag{22}$$

Equations (18)-(22) represent five boundary conditions in terms of the two dimensional stress resultants.

RESULTING SYSTEM OF EQUATIONS

The method of Fourier transform is applied to a similar problem with constant edge traction by Karr and Choi (1989). Here, a more general loading condition $P(x)$ can be applied and we use the three edge loadings discussed above as numerical examples. The development of the governing equations for general edge load can be performed in a similar manner; for completeness of this presentation the Fourier transforms of the stress resultants are presented in the Appendix.

Substituting equations (A.1)-(A.9) in the Appendix to the boundary conditions (18-22), a system of five by five equations can be derived in terms of the normalized variables:

$$A(\bar{\xi}) + \frac{2\nu}{15}\bar{\xi}^2[D(\bar{\xi}) + E(\bar{\xi})] = \frac{R_j}{\sigma_0}, \tag{23}$$

$$\begin{aligned} &-\frac{\nu}{3(1+\nu)}\bar{\xi}|\bar{\xi}|B(\bar{\xi}) - i\bar{\xi}\frac{4}{21}\sqrt{\bar{\xi}^2 + \frac{21}{2}}C(\bar{\xi}) \\ &+\left[1 + \frac{2}{21}(2-\nu)\bar{\xi}^2 - \frac{2(1-69\nu^2/70)}{63(1+\nu)}\bar{\xi}^2\mu^2\right]D(\bar{\xi}) \\ &+\left[1 + \frac{2}{21}(2-\nu)\bar{\xi}^2 - \frac{2(1-69\nu^2/70)}{63(1+\nu)}\bar{\xi}^2\hat{\mu}^2\right]E(\bar{\xi}) = 0, \end{aligned} \tag{24}$$

$$\begin{aligned} &-i\bar{\xi}^2\frac{\nu}{3(1+\nu)}B(\bar{\xi}) + \left(1 + \frac{4}{21}\bar{\xi}^2\right)C(\bar{\xi}) \\ &+i\bar{\xi}\sqrt{\bar{\xi}^2+\mu^2}\left[\frac{2}{21}(2-\nu) - \frac{2(1-69\nu^2/70)}{63(1+\nu)}\mu^2\right]D(\bar{\xi}) \\ &+i\bar{\xi}\sqrt{\bar{\xi}^2+\hat{\mu}^2}\left[\frac{2}{21}(2-\nu) - \frac{2(1-69\nu^2/70)}{63(1+\nu)}\hat{\mu}^2\right]E(\bar{\xi}) = 0, \end{aligned} \tag{25}$$

$$|\bar{\xi}|A(\bar{\xi}) - \bar{\xi}B(\bar{\xi}) + \frac{2\nu}{15}\bar{\xi}^2\left[\sqrt{\bar{\xi}^2+\mu^2}D(\bar{\xi}) + \sqrt{\bar{\xi}^2+\hat{\mu}^2}E(\bar{\xi})\right] = 0, \tag{26}$$

$$\sqrt{\bar{\xi}^2+\mu^2}D(\bar{\xi}) + \sqrt{\bar{\xi}^2+\hat{\mu}^2}E(\bar{\xi}) - i\bar{\xi}C(\bar{\xi}) = 0. \tag{27}$$

in which, ξ is the variable introduced through the Fourier transform, μ and $\hat{\mu}$ are complex conjugates as defined in Clark (1985), R_j is the Fourier transform of the edge loading P_j, and the overlined variables are the variables normalized with respect to a or c:

$$\bar{\xi} = c\xi, \qquad \bar{x} = x/a, \qquad \bar{y} = y/a.$$

Evaluating the integrals for the Fourier transforms of the three edge loadings (Gradshteyn and Ryzhik. 1980), we have:

$$R_1 \equiv \int_{-\infty}^{\infty} P_1(x)e^{i\xi x}dx = -a\sigma_0\sqrt{\pi}\left(\frac{2}{\xi a}\right)^{\frac{3}{2}}J_{\frac{3}{2}}(\xi a); \tag{28}$$

$$R_2 \equiv \int_{-\infty}^{\infty} P_2(x)e^{i\xi x}dx = -a\sigma_0\pi\frac{J_1(\xi a)}{(\xi a)}; \tag{29}$$

$$R_3 \equiv \int_{-\infty}^{\infty} P_3(x) e^{i\xi x} dx = -a\sigma_0 \pi J_0(\xi a). \qquad (30)$$

In equations (28)-(30), $J_{3/2}$, J_1 and J_0 represent the first kind Bessel functions of orders 3/2, 1 and 0. Substituting equations (28)-(30) into equation (23) we get:

$$A(\bar{\xi}) + \frac{2\nu}{15}\bar{\xi}^2[D(\bar{\xi}) + E(\bar{\xi})] = -a\sqrt{\pi}\left(\frac{2}{\bar{\xi}\gamma}\right)^{\frac{3}{2}} J_{\frac{3}{2}}(\bar{\xi}\gamma); \qquad (23a)$$

$$A(\bar{\xi}) + \frac{2\nu}{15}\bar{\xi}^2[D(\bar{\xi}) + E(\bar{\xi})] = -a\pi\frac{J_1(\bar{\xi}\gamma)}{(\bar{\xi}\gamma)}; \qquad (23b)$$

$$A(\bar{\xi}) + \frac{2\nu}{15}\bar{\xi}^2[D(\bar{\xi}) + E(\bar{\xi})] = -a\pi J_0(\bar{\xi}\gamma). \qquad (23c)$$

Equations (23 a,b,c)-(27) are the five normalized boundary condition equations involving five unknown functions $A(\bar{\xi}), B(\bar{\xi}), C(\bar{\xi}), D(\bar{\xi}), E(\bar{\xi})$.

NUMERICAL SCHEMES AND RESULTS

The five by five system of equations (23-27) is solved in terms of ξ explicitly using the symbolic software MAPLE. Having $A(\bar{\xi}), B(\bar{\xi}), C(\bar{\xi}), D(\bar{\xi}), E(\bar{\xi})$, the Fourier transform of the stress resultants $\bar{N}_{xx}, \bar{N}_{yy}, \bar{N}_{xy}, \bar{R}_{xx}, \bar{R}_{yy}, \bar{R}_{xy}, \bar{S}_x, \bar{S}_y$ and $\bar{T}$ (see equations A.1-A.9) can be evaluated numerically for a certain y location in the sheet for all ξ values in the integration range. Theoretically the range of integration for Fourier transform should be $-\infty < \xi < \infty$, but practically a smaller range can be used based on the shape of the integrand. Karr and Choi (1989) carried out their computation for the range of $-60 \le \xi \le 60$ and their solution is not stable as γ approaches zero. In this study, convergence study has been performed and it is found that the minimum converged upper and lower bounds for integrations are $\bar{\xi} = \pm 1000$. The stress resultants are then determined by integrations of the inverse Fourier transforms and finally the stresses throughout the entire sheet can be calculated using equations (1) and (2). Numerical integration is employed to evaluate the inverse Fourier transforms. The Bessel functions on the right hand sides of equations (23a.b,c) are also evaluated for each integration point (Watson, 1966). The integrals for the first two kinds of loadings are relatively easy to evaluate and the computation time used is moderate. The third kind of loading, because of the singularity of the stress distribution at $x = \pm a$, needs more integration points inside the upper and lower bounds and therefore requires more computation time to obtain satisfactory answers. Several Fortran codes have been developed to perform the computations.

The numerical results for the stress $\bar{\sigma}_y(\bar{x}, \bar{y}, 0)$ are shown in Fig. 3 for cases with the aspect ratio $\gamma = 1.5$ and Poisson's ratio $\nu = 0.3$. Figure 3(a) shows the results for the parabolic distribution of the applied traction stress. Results for loading conditions $P_2(x)$ and $P_3(x)$ are shown in Fig. 3(b) and 3(c) respectively. The stress in the middle layer of the sheet $\bar{\sigma}_y(0, \bar{y}, 0)$ decays more rapidly with respect to $\bar{y}$ for the parabolic loading than for the loadings $P_2(x)$ and $P_3(x)$. It is also obvious that with the improved integration range for ξ, the calculated stress distribution presented here are more accurate than that of Karr and Choi (1989) and the stress distributions for $\bar{y} = 0$ converge to those prescribed in equations (12)-(14).

The results for the stress $\bar{\sigma}_x(\bar{x}, \bar{y}, 0)$ are shown in Fig. 4. For all these loading cases, $P_1(x), P_2(x)$ and $P_3(x)$, the stresses $\bar{\sigma}_x$ decay more rapidly with respect to $\bar{y}$ than do the stresses $\bar{\sigma}_y$. It is also interesting to note the zone of tensile stress at the edge of the sheet ($\bar{y} = 0$) just beyond the edge of the loaded area. These tensile stresses are in the order of one tenth of the applied traction stress.

Figure 5(a,b,c) shows the transverse normal stress $\bar{\sigma}_z(\bar{x}, \bar{y}, 0)$ developed for the three kinds of loading conditions for an aspect ratio $\gamma = 1.5$ and Poisson's ratio $\nu = 0.3$. It is worthwhile to notice that a significant amount of tensile stress $\bar{\sigma}_z$ builds up near the location of ($\bar{x} = \pm 1, \bar{y} = 0, \bar{z} = 0$) on the edge of the sheet for all the three kinds of loadings. Thus if the sheet is made of brittle material, a spalling mode of failure may initiate at these locations. It is also noted that $\bar{\sigma}_z(\bar{x}, \bar{y}, 0)$ decays more rapidly with respect to $\bar{y}$ than the other two normal stresses and therefore the state of stress away from the indentor is very closed to that of plane stress. This indicates that the tenth-order theory correction to a plane problem represent an edge zone correction which is only important within a certain distance from the indentor.

In order to verify the results obtained by the tenth-order theory, finite element analyses of the same problem have also been performed using the commercial FEA code ABAQUS. Eight node three dimensional brick element C3D8 is used near the contact region. The far field is modeled with an eight node infinite element CIN3D8. Only one-quarter of the semi-infinite sheet is modeled and symmetry conditions are imposed on the planes of $x = 0$ and z=0. The model is shown in Fig. 6. The above discussed three loading conditions are applied as pressure distributions along the plate edge y=0. Results compared with those of the tenth-order theory are plotted as discrete points in Fig. 3(a,b,c)-Fig. 5(a,b,c). As shown in Fig. 3(a,b,c) and Fig. 4(a,b,c), very good correlations are achieved between the tenth-order theory and the finite element analysis for normal stresses $\bar{\sigma}_x$ and $\bar{\sigma}_y$ on the symmetry plane z=0. However, results for $\bar{\sigma}_z$ between the two methods are not consistent in magnitude, as shown in Fig.

5(a,b,c). This is due to the fact that only 4 elements are used in the through thickness direction. Should more elements be used in the z direction, more accurate results will be achieved.

By examining the FEA results, it is also found that the assumed parabolic distributions of σ_x and σ_y along z direction are very close to the true stress distributions, with the magnitude of R_{yy} being very small throughout the sheet and eventually becoming zero at the plate edge y=0. This is consistent with equation (19) and it ensures that the resulted stress distribution on edge y=0 converges to the prescribed condition of σ_y being constant through the thickness.

CONCLUSIONS

We now discuss the effect of aspect ratio γ. If the plate thickness 2c is much smaller than the loading region $2a$, γ goes to infinity and the solution degenerates to the solution of a plane stress case as discussed previously. On the other hand, if the plate thickness 2c is very large or if the loading region is very small, i.e. $a \ll c$, γ goes to zero. Under such conditions, the assumed stress distribution in the z-direction no longer represents the true stress distribution and therefore the limiting solution should not converge to a plane strain case. This conclusion is in contrast to Karr and Choi's $\gamma \to 0$ conclusion. In this study, larger integration limit and more integration points are used to achieve more stable and accurate numerical results as γ approaches zero. Moreover, as shown in the following discussions, the same limit solution is obtained for different loading conditions.

The stress $\bar{\sigma}_x(0, 0, 0)$ at the center of the edge of the sheet for four loading cases is shown in Fig. 7 as a function of the aspect ratio γ. Poisson's ratio is $\nu = 0.3$. The uniform loading case addressed by Karr and Choi (1989) is shown together with the three loading cases addressed here. The peak stresses occur near an aspect ratio of $\gamma \cong 0.5$ for all loading cases; the maximum compressive stresses are approximately 20% higher than the value obtained for plane stress and plane strain in which the value of $\bar{\sigma}_x(0, 0, 0)$ is unity (Timoshenko and Goodier, 1970). For all loading conditions the limit value of $\bar{\sigma}_x(0, 0, 0) = -1.09$ is approached as $\gamma \to 0$. Since larger ξ range and more integration points have been used in this study, the limit stress values as γ approaching zero can be carried out very close to γ=0 without the numerical instabilities experienced by Karr and Choi(1989).

Results for the stress at the corner of the plate, $\bar{\sigma}_x(0, 0, \pm c)$ are shown in Fig. 8. The minimum compressive stresses occur in the range of γ between 0.3 and 0.8 depending on the loading conditions. These minimum compressive stresses range from about 65% of the applied stress to about 56% of the applied stress for load condition $P_3(x)$. The limit condition for $\gamma \to 0$ is $\bar{\sigma}_x(0, 0, \pm c) = -0.815$ for all three loading conditions.

The transverse normal stress at the center of the loading is shown as a function of γ in Fig. 9. No significant tensile stresses develop at this point for loading conditions $P_1(x)$ or $P_2(x)$. The limiting value for $\bar{\sigma}_z(0, 0, 0)$ is -0.809. Significant transverse stresses essentially vanish for aspect ratios above 3 or 4.

In addressing the transition from plane stress, three dimensional effects regarding $\bar{\sigma}_x$ are initially more pronounced for loading condition $P_1(x)$, followed by $P_2(x)$, the uniform loading, and the condition $P_3(x)$. However, as the aspect ratio continues to decrease, below say $\gamma = 1.0$, the relative influence of the three dimensional effects changes. The loading condition $P_3(x)$ shows the most significant three dimensional effects on $\bar{\sigma}_x(0, 0, \pm c)$ and $\bar{\sigma}_x(0, 0, 0)$. Deviation from plane stress occurs less rapidly (as γ decreases) for $\bar{\sigma}_z(0, 0, 0)$ than for $\bar{\sigma}_x(0, 0, \pm c)$ or $\bar{\sigma}_x(0, 0, 0)$. For example, for loading condition $P_1(x)$, a change in $\bar{\sigma}_x$ of 10% of the applied stress occurs for an aspect ratio of 3; a change in $\bar{\sigma}_z(0, 0, 0)$ of 10% of the applied stress occurs near a value of $\gamma = 1.5$.

The solutions for $\sigma_x(0, 0, 0)$ and $\sigma_z(0, 0, 0)$ obtained in Fig. 7, 8 and 9 for vanishing aspect ratio are different from the plane strain solutions suggested by Karr and Choi (1989). Again, the underlying assumptions of the tenth-order theory involve a prescribed parabolic distribution of the transverse stress which vanishes at $z = \pm c$. These assumptions preclude obtaining the plane strain condition for which it is assumed that there is no functional dependency with respect to the z coordinate.

REFERENCES

Barber, J.R., 1992, *Elasticity*. Kluwer Academic Publishers, the Netherlands.

Clark, R.A.and Reissner, E., 1984, "A tenth-order theory of stretching of transversely isotropic sheets", *ZAMP*. Vol. 35, pp. 883-889.

Clark, R.A., 1885, "Three-dimensional corrections for a plane stress problem", *Int. J. Solids Structures.*, Vol. 21, pp. 3-10.

Gradshteyn, I.S. and Ryzhik, I.M., 1980, *Table of integrals, series and products, Corrected and enlarged edition*, Academic Press Inc., New York.

Karr, D.G. and Choi, S.K., 1989, "Three-dimensional elasticity solutions for edge loaded semi-infinite sheets", *Z.angew.Math.Mech*, Vol. 69, pp. 329-337.

Karr, D.G. and Sun, X., 1995, "Damage Evolution During Impact of an Ice Bar with Lateral Confinement", *Int. J. of Offshore and Polar Engineering*, Vol. 5, No. 1, pp. 23-31.

Reissner, E., 1942, "On the calculation of three-dimensional corrections for the two-dimensional theory of plane stress", In: *Proc. 15th Semi-Annual Eastern Photoelasticity conference*, pp. 23-31.

Sneddon, I.N., 1951, *Fourier transforms. 2nd edition*, McGraw Hill Book Co., Inc., New York.

Timoshenko, S.P. and Goodier, J.N., 1970, *Theory of elasticity*. 3rd edition, McGraw Hill Book Co., Inc, New York

Watson, G.N., 1966, *A treatise on the theory of Bessel functions*, Cambridge, Cambridge U.K.

APPENDIX: FOURIER TRANSFORM METHOD

The Fourier transform and its inverse transform are defined to be (Sneddon, 1951):

$$\bar{\varphi}(\xi, y) = \int_{-\infty}^{\infty} e^{i\xi x}\varphi(x, y)dx \qquad \varphi(x, y) = \frac{1}{2\pi}\int_{-\infty}^{\infty} e^{-i\xi x}\bar{\varphi}(\xi, y)d\xi$$

As shown in Karr and Choi (1989), the Fourier transforms of the stress resultants expressed in terms of the five functions $A(\xi)$, $B(\xi)$, $C(\xi)$, $D(\xi)$ and $E(\xi)$ are:

$$\bar{N}_{xx}(\xi, y) = \frac{N_0}{\xi^2}\{2\xi B(\xi)|\xi| - \xi^2[A(\xi) + \xi B(\xi)y]\}e^{-|\xi|y} - \frac{2\nu}{15}c^2 N_0$$

$$\left\{\left[\xi^2 + \left(\frac{\mu}{c}\right)^2\right]D(\xi)e^{-y\sqrt{\xi^2+(\mu/c)^2}} + \left[\xi^2 + \left(\frac{\hat{\mu}}{c}\right)^2\right]E(\xi)e^{-y\sqrt{\xi^2+(\hat{\mu}/c)^2}}\right\}, \tag{A.1}$$

$$\bar{N}_{yy}(\xi, y) = N_0[A(\xi) + \xi y B(\xi)]e^{-|\xi|y} + \frac{2\nu}{15}c^2\xi^2 N_0$$

$$\left[D(\xi)e^{-y\sqrt{\xi^2+(\mu/c)^2}} + E(\xi)e^{-y\sqrt{\xi^2+(\hat{\mu}/c)^2}}\right]. \tag{A.2}$$

$$\bar{N}_{xy} = -\frac{iN_0}{\xi}\{\xi B(\xi) - |\xi|[A(\xi) + \xi y B(\xi)]\}e^{-|\xi|y} +$$

$$i\xi\frac{2\nu}{15}c^2 N_0\sqrt{\xi^2+(\mu/c)^2}D(\xi)e^{-y\sqrt{\xi^2+(\mu/c)^2}} +$$

$$i\xi\frac{2\nu}{15}c^2 N_0\sqrt{\xi^2+(\hat{\mu}/c)^2}E(\xi)e^{-y\sqrt{\xi^2+(\hat{\mu}/c)^2}} \tag{A.3}$$

Additionally,

$$\frac{1}{N_0}\bar{R}_{xx} = 2c^2\frac{\nu}{6(1+\nu)}\xi|\xi|B(\xi)e^{-|\xi|y} +$$

$$\left\{1 - \frac{2}{21}c^2\left(\xi^2 + \frac{\mu^2}{c^2}\right)\left[(2-\nu) - \frac{1-\frac{69}{70}\nu^2}{3(1+\nu)}\mu^2\right]\right\}D(\xi)e^{-y\sqrt{\xi^2+\left(\frac{\mu}{c}\right)^2}}$$

$$+\left\{1 - \frac{2}{21}c^2\left(\xi^2 + \frac{\hat{\mu}^2}{c^2}\right)\left[(2-\nu) - \frac{1-\frac{69}{70}\nu^2}{3(1+\nu)}\hat{\mu}^2\right]\right\}E(\xi)e^{-y\sqrt{\xi^2+\left(\frac{\hat{\mu}}{c}\right)^2}}$$

$$+ i\xi\frac{4c^2}{21}\sqrt{\xi^2 + \frac{21}{2c^2}}C(\xi)e^{-y\sqrt{\xi^2+\frac{21}{2c^2}}}, \tag{A.4}$$

$$\frac{1}{N_0}\bar{R}_{yy} = -2c^2\frac{\nu}{6(1+\nu)}\xi|\xi|B(\xi)e^{-|\xi|y} +$$

$$\left\{1 + \frac{2}{21}c^2\xi^2\left[(2-\nu) - \frac{1-69\nu^2/70}{3(1+\nu)}\mu^2\right]\right\}D(\xi)e^{-y\sqrt{\xi^2+(\mu/c)^2}} +$$

$$\left\{1 + \frac{2}{21}c^2\xi^2\left[(2-\nu) - \frac{1-69\nu^2/70}{3(1+\nu)}\hat{\mu}^2\right]\right\}E(\xi)e^{-y\sqrt{\xi^2+(\hat{\mu}/c)^2}}$$

$$-i\xi\frac{4c^2}{21}\sqrt{\xi^2 + \frac{21}{2c^2}}C(\xi)e^{-y\sqrt{\xi^2+\frac{21}{2c^2}}}, \tag{A.5}$$

$$\frac{1}{N_0}\bar{R}_{xy} = -2i\xi^2\frac{\nu}{6(1+\nu)}c^2 B(\xi)e^{-|\xi|y} +$$

$$i\xi c^2\sqrt{\xi^2 + \frac{\mu^2}{c^2}}D(\xi)\frac{2}{21}\left[2 - \nu - \frac{1-69\nu^2/70}{3(1+\nu)}\mu^2\right]e^{-y\sqrt{\xi^2+(\mu/c)^2}}$$

$$+ i\xi c^2\sqrt{\xi^2 + \frac{\hat{\mu}^2}{c^2}}E(\xi)\frac{2}{21}\left[2 - \nu - \frac{1-69\nu^2/70}{3(1+\nu)}\hat{\mu}^2\right]e^{-y\sqrt{\xi^2+(\hat{\mu}/c)^2}}$$

$$-\frac{2c^2}{21}\xi^2 C(\xi)e^{-y\sqrt{\xi^2+\frac{21}{2c^2}}}. \tag{A.6}$$

and $$\frac{1}{N_0}\bar{S}_x = i\xi\left[D(\xi)e^{-y\sqrt{\xi^2+(\mu/c)^2}} + E(\xi)e^{-y\sqrt{\xi^2+(\hat{\mu}/c)^2}}\right]$$

$$+\sqrt{\xi^2 + \frac{21}{2c^2}}C(\xi)e^{-y\sqrt{\xi^2+\frac{21}{2c^2}}}. \tag{A.7}$$

$$\frac{1}{N_0}\bar{S}_y = -i\xi C(\xi)e^{-y\sqrt{\xi^2+\frac{21}{2c^2}}} +$$

$$\sqrt{\xi^2+\left(\frac{\mu}{c}\right)^2}D(\xi)e^{-y\sqrt{\xi^2+\left(\frac{\mu}{c}\right)^2}} + \sqrt{\xi^2+\left(\frac{\hat{\mu}}{c}\right)^2}E(\xi)e^{-y\sqrt{\xi^2+\left(\frac{\hat{\mu}}{c}\right)^2}} \quad (A.8)$$

$$\frac{1}{N_0}\bar{T} = -\frac{1}{c^2}\left[\mu^2 D(\xi)e^{-y\sqrt{\xi^2+(\mu/c)^2}} + \hat{\mu}^2 E(\xi)e^{-y\sqrt{\xi^2+(\hat{\mu}/c)^2}}\right]. \quad (A.9)$$

In equations (A.1)-(A.9), the notations $N_0 = 2c\sigma_0$, $\mu^2 = (-A_2 + i\sqrt{4A_1 - A_2^2})/(2A_1)$ have been introduced and $\hat{\mu}^2$ is the complex conjugate of μ^2.

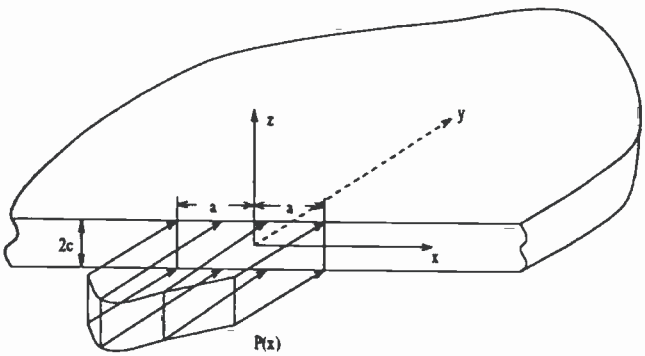

Fig. 1 Semi-infinite sheet with compressive edge loading.

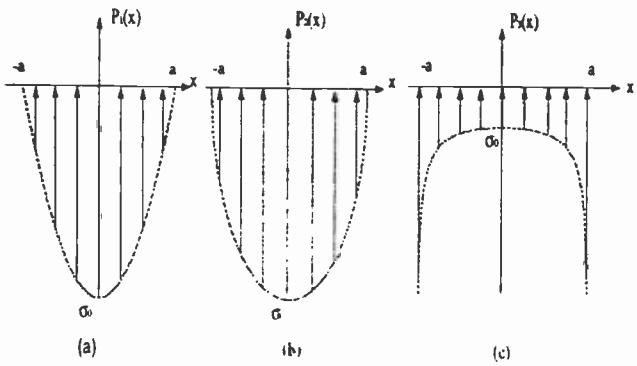

Fig. 2 Three kinds of loading conditions $P_i(x)$.

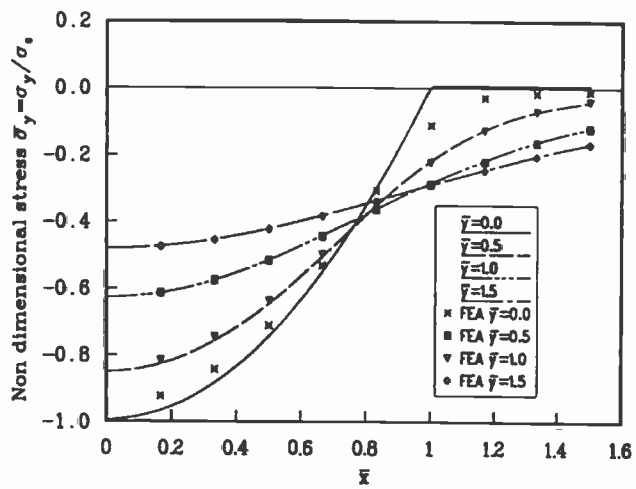

Fig. 3(a) $\bar{\sigma}_y(\bar{x},\bar{y},0)$ for γ=1.5 and ν=0.3 for loading condition $P_1(x)$.

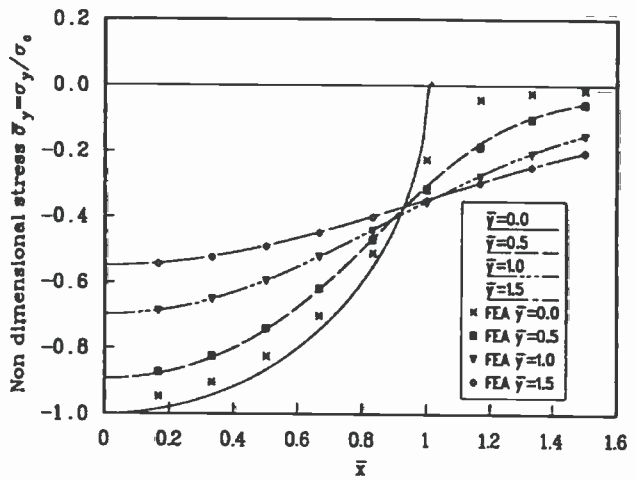

Fig. 3(b) $\bar{\sigma}_y(\bar{x},\bar{y},0)$ for γ=1.5 and ν=0.3 for loading condition $P_2(x)$.

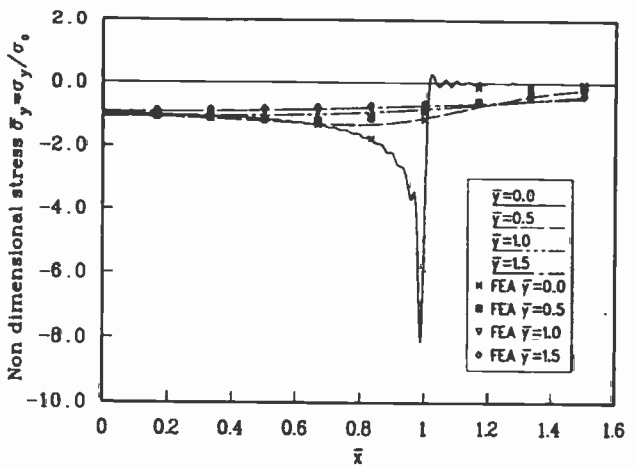

Fig. 3(c) $\bar{\sigma}_y(\bar{x},\bar{y},0)$ for γ=1.5 and ν=0.3 for loading condition $P_3(x)$.

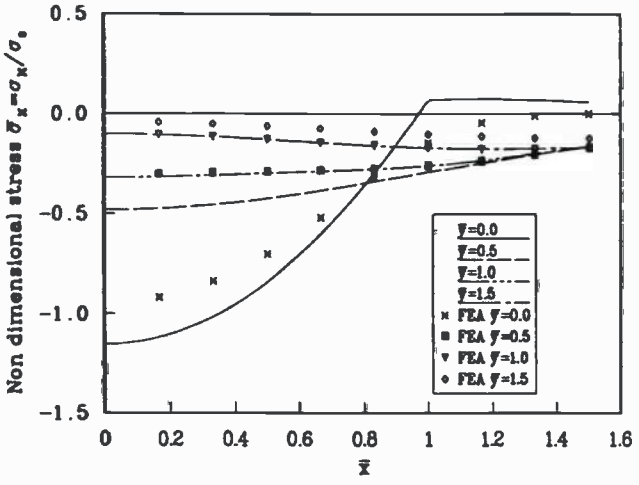

Fig. 4(a) $\bar{\sigma}_x(\bar{x},\bar{y},0)$ for γ=1.5 and ν=0.3 for loading condition $P_1(x)$.

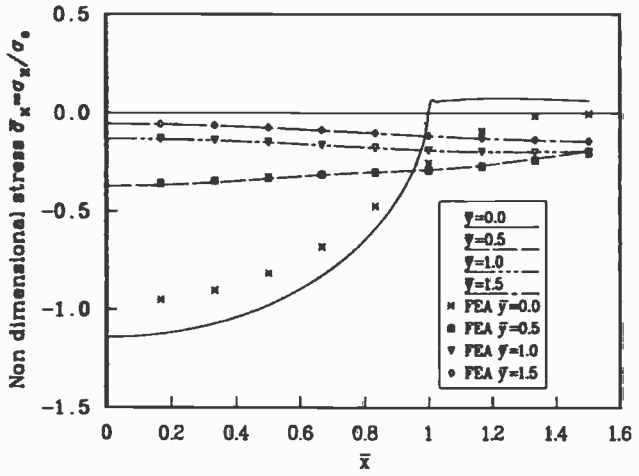

Fig. 4(b) $\bar{\sigma}_x(\bar{x},\bar{y},0)$ for γ=1.5 and ν=0.3 for loading condition $P_2(x)$.

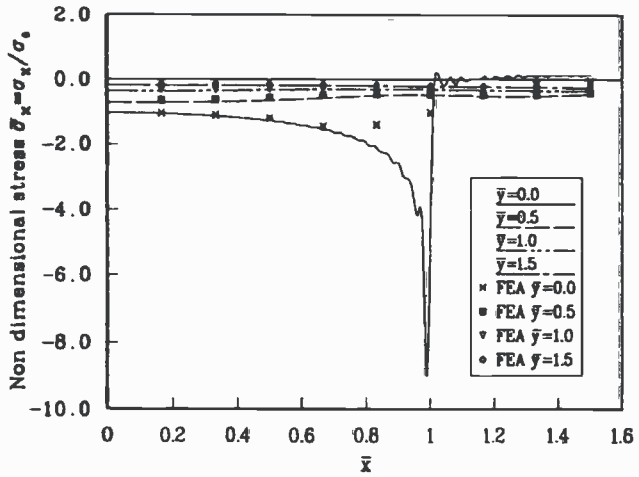

Fig. 4(c) $\bar{\sigma}_x(\bar{x},\bar{y},0)$ for γ=1.5 and ν=0.3 for loading condition $P_3(x)$

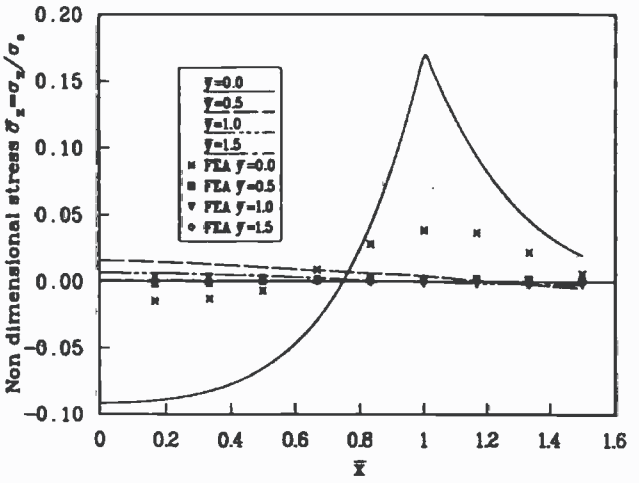

Fig. 5(a) $\bar{\sigma}_z(\bar{x},\bar{y},0)$ for γ=1.5 and ν=0.3 for loading condition $P_1(x)$.

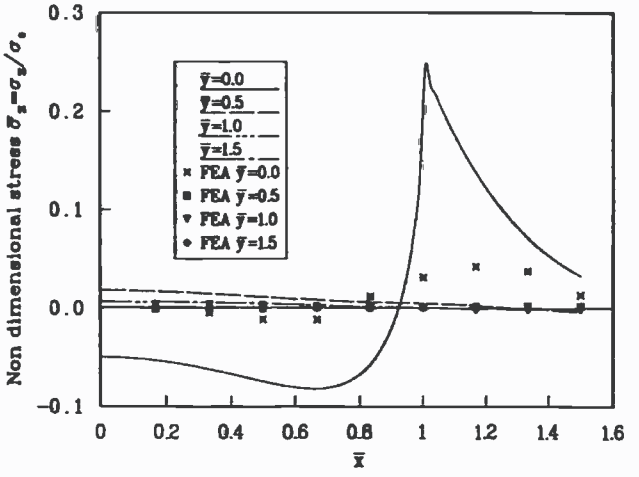

Fig. 5(b) $\bar{\sigma}_z(\bar{x},\bar{y},0)$ for γ=1.5 and ν=0.3 for loading condition $P_2(x)$.

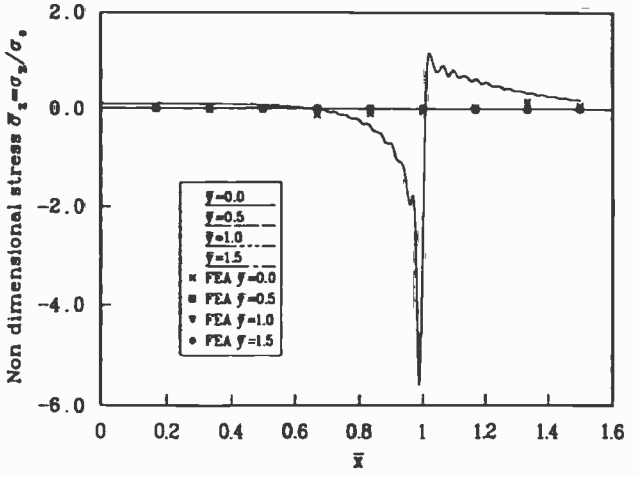

Fig. 5(c) $\bar{\sigma}_z(\bar{x},\bar{y},0)$ for γ=1.5 and ν=0.3 for loading condition $P_3(x)$.

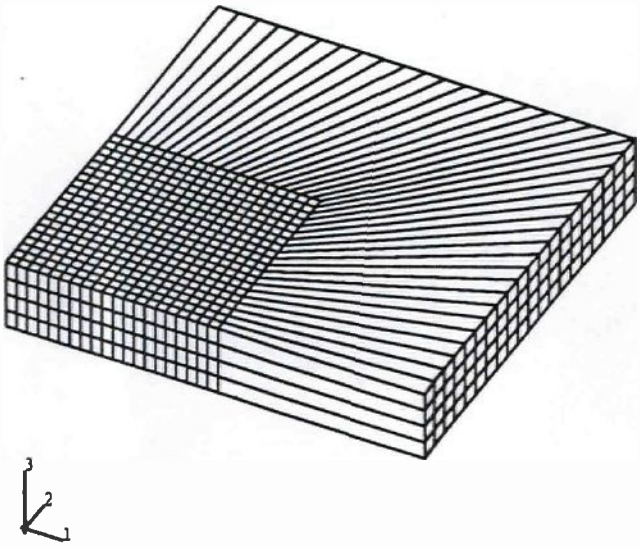

Fig. 6 Finite element mesh used for analysis.

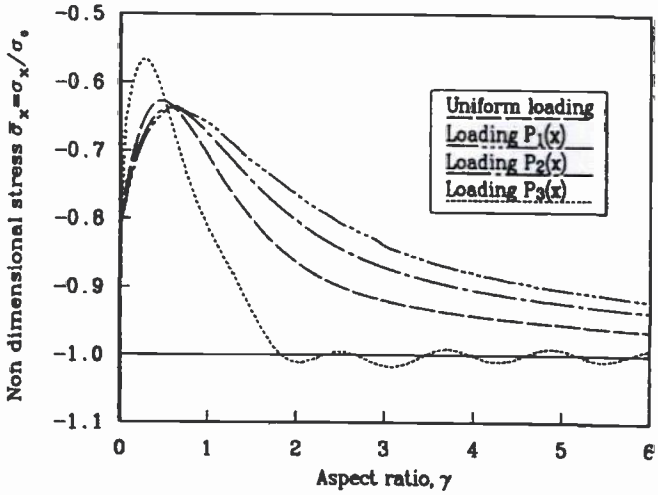

Fig.8 $\bar{\sigma}_x(0,0,\pm c)$ versus aspect ratio γ for ν=0.3.

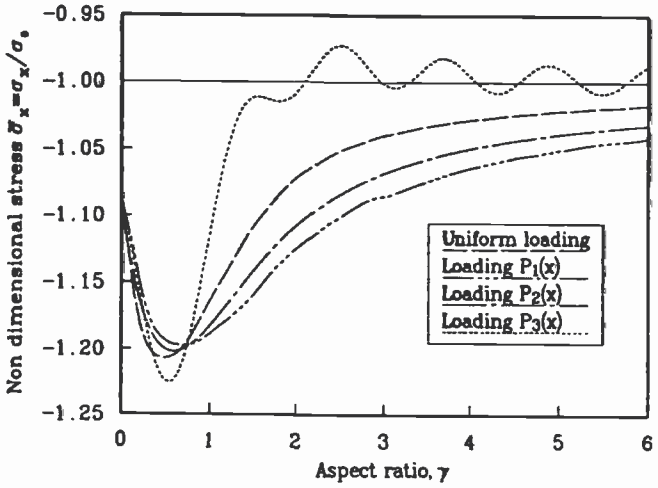

Fig.7 $\bar{\sigma}_x(0,0,0)$ versus aspect ratio γ for ν=0.3.

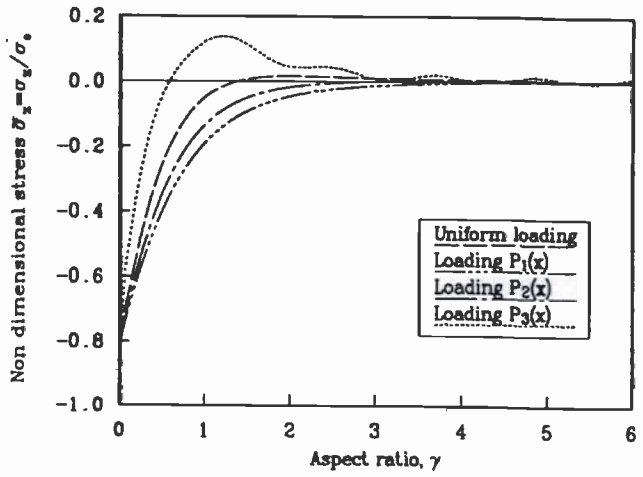

Fig.9 $\bar{\sigma}_z(0,0,0)$ versus aspect ratio γ for ν=0.3.